

Journal of Biomedical Optics

SPIDigitalLibrary.org/jbo

Compressed sensing based virtual- detector photoacoustic microscopy *in vivo*

Jing Meng
Chengbo Liu
Jiaxiang Zheng
Riqiang Lin
Liang Song

Compressed sensing based virtual-detector photoacoustic microscopy *in vivo*

Jing Meng,^a Chengbo Liu,^b Jiayang Zheng,^b Riqiang Lin,^b and Liang Song^{b,*}

^aQufu Normal University, College of Computer Science, 80 Yantai Road North, Rizhao 276826, China

^bShenzhen Institutes of Advanced Technology, Chinese Academy of Sciences, Institute of Biomedical and Health Engineering, 1068 Xueyuan Boulevard, Shenzhen 518055, China

Abstract. Photoacoustic microscopy (PAM) is becoming a vital tool for various biomedical studies, including functional and molecular imaging of cancer. However, due to the use of a focused ultrasonic transducer for photoacoustic detection, the image quality of conventional PAM degrades rapidly away from the ultrasonic focal zone. To improve the image quality of PAM for out-of-focus regions, we have developed compressed sensing based virtual-detector photoacoustic microscopy (CS-PAM). Through phantom and *in vivo* experiments, it has been demonstrated that CS-PAM can effectively extend the depth of focus of PAM, and thus may greatly expand its potential biomedical applications. © 2014 Society of Photo-Optical Instrumentation Engineers (SPIE) [DOI: [10.1117/1.JBO.19.3.036003](https://doi.org/10.1117/1.JBO.19.3.036003)]

Keywords: photoacoustic imaging; medical and biological imaging; compressed sensing; virtual-point detector.

Paper 130912R received Dec. 28, 2013; revised manuscript received Jan. 28, 2014; accepted for publication Jan. 29, 2014; published online Mar. 5, 2014.

1 Introduction

Photoacoustic tomography (PAT) can provide multiscale, multi-contrast imaging of intact biological tissue *in vivo*, demonstrating broad applications in both preclinical and clinical studies.^{1–3} Photoacoustic microscopy (PAM), using a focused single-element ultrasonic transducer for photoacoustic detection, is one form of PAT that can offer high-resolution deep-tissue imaging beyond the optical ballistic regime.⁴ Up to now, PAM has found important applications in both functional and molecular imaging of cancer.^{4,5} In addition, recent progress in PAM technology has demonstrated several first-of-its-kind *in vivo* applications, including label-free photoacoustic flowoxigraphy of individual cells⁶ and the imaging of slow blood flow in deep tissue.⁷ However, the image quality of conventional PAM degrades rapidly when the imaging targets are away from the ultrasonic focal zone. To overcome this limitation, a virtual detector technique was developed, shown to improve the image quality of PAM for out-of-focus regions.⁸ As this technique assumes “point-like” detection, it would work most effectively if the dimension of the virtual detector is $\leq \lambda_0/2$ (λ_0 is the center wavelength of the ultrasonic transducer) and the divergence angle of the virtual detector reaches $\pi/2$, when conventional back-projection reconstruction is used. However, in reality, these requirements can hardly be satisfied rigorously. Recently, a new reconstruction method based on interpolated model-matrix inversion (IMMI) was developed, in which the virtual detector was treated as a finite-size element (instead of a point), leading to improved reconstruction accuracy.⁹ In addition, a Bessel beam-based method was developed to improve the spatial resolution of out-of-focus regions for a particular form of PAM—optical-resolution PAM.¹⁰

Compressed sensing (CS) can recover sparse signals from under-sampled measurements.¹¹ Compared with conventional back-projection reconstruction, CS-based reconstruction was

demonstrated to significantly improve PAT image quality in previous studies, when the number of measurements was fewer than that required by the Nyquist sampling theorem.^{12,13} In this study, to improve the performance of the virtual detector technique, we have developed a compressed sensing based virtual-detector photoacoustic microscopy (CS-PAM). Through phantom and *in vivo* experiments, it has been shown that, even with a virtual detector of a relatively small divergence angle compared to $\pi/2$ (which is the case for most PAM systems), CS-PAM can still significantly improve the image quality of out-of-focus regions, over both conventional PAM and back projection-based virtual-detector PAM (BP-PAM).

2 Methods

2.1 Imaging System

The PAM system used in this study is shown in Fig. 1(a). A tunable pulsed optical parametric oscillator (OPO) laser (Vibrant 355 II HE, Opotek, Carlsbad, California) with a repetition rate of 10 Hz and a pulse width of 5 ns was used to illuminate the imaging targets through a custom-made light delivery system. A spherically focused ultrasonic transducer (V315, Olympus, Tokyo, Japan) was used to sense the excited photoacoustic pressures from the targets. The electrical signals from the transducer were then amplified and acquired by a data acquisition card at a speed of 50 MS/s for digitization. Further details of the system can be found in our previous publications,¹⁴ and thus are not repeated here. Figure 1(b) illustrates the basic principles of virtual-detector PAM. In short, the focal point of the ultrasonic transducer was treated as a virtual detector, with its divergence angle determined primarily by the NA of the transducer. Through mechanical scanning of this virtual detector, it resembles the detection of a linear ultrasonic array and thus can recover the information of the out-of-focus regions

*Address all correspondence to: Liang Song, E-mail: liang.song@siat.ac.cn

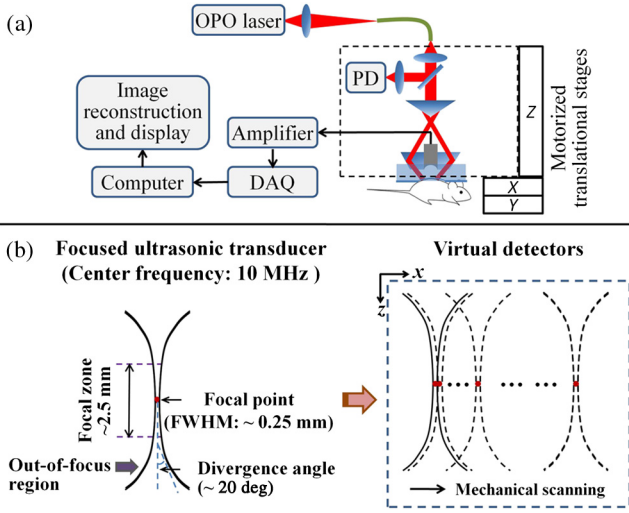


Fig. 1 (a) Overall architecture of the photoacoustic microscopy (PAM) system and (b) illustration of the concept of virtual-detector PAM. PD, photodiode; FWHM, full width at half maximum.

through reconstruction. In this study, the ultrasonic transducer has a center frequency of 10 MHz, a diameter of 19 mm, and a focal length of ~ 25 mm. As a result, the full width half maximum (FWHM) of the focal point of the transducer is ~ 250 μm , with a focal zone of ~ 2.5 mm, and a divergence angle of ~ 20 deg [Fig. 1(b)].

2.2 Reconstruction Model

In general, during photoacoustic wave generation, the acoustic pressure $p(\mathbf{r}, t)$ at position \mathbf{r} and time t satisfies the wave equation:

$$\left(\nabla^2 - \frac{1}{c^2} \frac{\partial^2}{\partial t^2}\right) p(\mathbf{r}, t) = -p_0(\mathbf{r}) \frac{d\delta(t)}{dt}, \quad (1)$$

where $p_0(\mathbf{r})$ is the initial photoacoustic pressure excited by the laser (or electromagnetic) pulse $\delta(t)$ and c is the speed of sound. The back-projection reconstruction used in our work, which incorporates the effect of the acceptance (divergence) angle, can be described by the following equation:

$$p_0^b(\mathbf{r}) = \sum_{d=1}^M w_d b(\mathbf{r}^{(d)}, \bar{t}), \quad \bar{t} = |\mathbf{r} - \mathbf{r}^{(d)}|, \quad (2)$$

where $b(\mathbf{r}^{(d)}, \bar{t}) = 2p(\mathbf{r}^{(d)}, \bar{t}) - 2\bar{t}\partial p(\mathbf{r}^{(d)}, \bar{t})/\partial \bar{t}$, $\bar{t} = ct$, $\mathbf{r}^{(d)}$ represents the position of the d 'th detector, $\theta(\mathbf{r}^{(d)})$ represents the acceptance angle of detector d , and w_d is an angle weighted factor of the d 'th detector.¹⁵

On the other hand, CS is known to recover sparse or compressible signals with under-sampled measurements. To apply CS-based reconstruction, it is required that the signals shall possess sparsity in certain domains. Fortunately, most medical images are sparse in certain domains by finding an appropriate sparse transform $\psi: \mathbf{x} = \psi\theta$, where θ is the original image and \mathbf{x} is the transformed one.

In PAT, if the measurement data from the ultrasonic transducers is \mathbf{y} , the measurement matrix corresponding to the imaging system is \mathbf{K} , then we have $\mathbf{y} = \mathbf{K}\theta = \mathbf{K}\Psi^{-1}\mathbf{x}$. When CS is incorporated into the photoacoustic imaging process,

the reconstruction with sparse transform ψ can be implemented by solving the following constrained optimization problem:

$$\min \|\mathbf{x}\|_1 \quad \text{s.t.} \quad \mathbf{y} = \mathbf{K}\Psi^{-1}\mathbf{x}. \quad (3)$$

It is noteworthy that, the incoherence between the measurement matrix and the sparse transform is another important condition to guarantee the successful application of CS. In previous works, this condition has been proven to be satisfied in photoacoustic reconstruction.^{16,17}

To recover the photoacoustic images of the physically out-of-focus regions in PAM, a CS-based reconstruction model according to Eq. (3) was developed in our work

$$\arg \min_{\mathbf{x}} F = \|\mathbf{K}_{\text{angle}}\Psi^{-1}\mathbf{x} - \mathbf{y}\|_2^2 + \alpha\|\mathbf{x}\|_1 + \beta\text{TV}(\Psi^{-1}\mathbf{x}). \quad (4)$$

Equation (4) can also be written as

$$\arg \min_{\theta} F = \|\mathbf{K}_{\text{angle}}\theta - \mathbf{y}\|_2^2 + \alpha\|\Psi\theta\|_1 + \beta\text{TV}(\theta). \quad (5)$$

In Eq. (4), Ψ is the sparse transform—in this study, a four-level Daubechies wavelet transform is used. In addition to the item of l_1 norm in a sparse domain, the total variation penalty of the signals is also incorporated into the objective function F to improve the reconstruction accuracy. Further, α and β (0.06 and 0.1, respectively, in this study) are the regularization parameters determining the trade-off between the data consistency and the sparsity, which should be determined appropriately. Overweighed values could result in distortion of the reconstruction. On the contrary, if their proportions to the objective function were too small, their support would become ineffective. In our experiments, they were empirically determined by trying different combinations and choosing the optimal ones. Finally, $\mathbf{K}_{\text{angle}}$ is the measurement matrix incorporating the effect of the divergence angle, which is defined as

$$K_{\text{angle}}(m, t)_{(i,j)} = \begin{cases} \frac{1}{2\pi c} \delta\left(t - \frac{|\mathbf{r}_{ij} - \mathbf{r}_m|}{c}\right), & \tan^{-1} \left\{ \frac{\text{abs}\left[\frac{r_{ij}(x) - r_m(x)}{r_{ij}(z) - r_m(z)}\right]}{\text{abs}\left[\frac{r_{ij}(x) - r_m(x)}{r_{ij}(z) - r_m(z)}\right]}\right\} \leq \theta \\ 0, & \tan^{-1} \left\{ \frac{\text{abs}\left[\frac{r_{ij}(x) - r_m(x)}{r_{ij}(z) - r_m(z)}\right]}{\text{abs}\left[\frac{r_{ij}(x) - r_m(x)}{r_{ij}(z) - r_m(z)}\right]}\right\} > \theta \end{cases} \quad (6)$$

where \mathbf{r}_{ij} represents the Cartesian coordinates of the image pixels, \mathbf{r}_m represents the positions of the virtual detector, c is the sound speed, p is the number of virtual detectors, Δt is the sampling interval, q_s is the number of sampling points for each A-line in the time domain, $r_{ij}(x)$ and $r_{ij}(z)$ represent the positions of the image pixels at x - and z -axes [Fig. 1(b)], respectively, and θ is the divergence angle of the virtual detector. To solve Eq. (5), a nonlinear conjugate gradient descent method was adopted, in which the gradient computation of the objection function can be found in Ref. 18.

3 Experimental Results

3.1 Phantom Results

To validate the effectiveness of CS-PAM, phantom experiments were performed. To fabricate the phantom, three human hairs

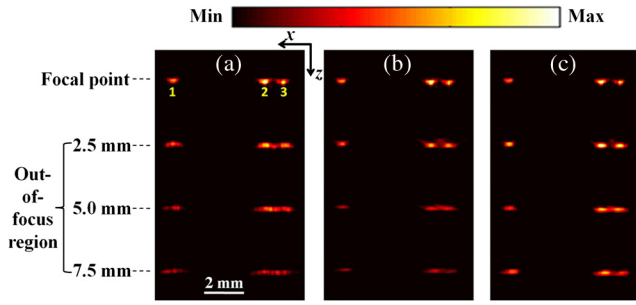


Fig. 2 Photoacoustic images of the hair phantom. (a) Directly acquired photoacoustic B-scan images of in-focus and out-of-focus hairs; (b) and (c) B-scan images reconstructed with BP-PAM and CS-PAM, respectively.

with diameters of $\sim 50 \mu\text{m}$ were fixed in parallel on the surface of a hollow plastic holder, with a $\sim 4.2 \text{ mm}$ separation between hair-1 and hair-2, and a $\sim 0.9 \text{ mm}$ separation between hair-2 and hair-3. In a series of experiments, the height of the ultrasonic transducer was varied (while the optical illumination on the hairs was unchanged), so that the phantom was imaged under both in-focus and out-of-focus circumstances. For the out-of-focus cases, the phantom was placed at 2.5, 5.0, and 7.5 mm away from the focal point, respectively. To complete a B-scan for each case, the imaging head was mechanically scanned along x , with a step size of $50 \mu\text{m}$ and a total scanning range of 6.4 mm.

Figure 2(a) shows the directly acquired PAM images under both in-focus and out-of-focus conditions. As expected, the photoacoustic images get blurred more and more when the hairs are away from the ultrasonic focal point. However, upon performing image reconstruction with either back-projection or compressed-sensing strategy, using the scanning focal point as

virtual detectors, the spatial resolution and contrast of the photoacoustic images of the out-of-focus hairs are clearly improved [Figs. 2(b) and 2(c)]. Further, compared with that using BP-PAM, the separation between hair-2 and hair-3 is resolved even better using CS-PAM. Finally, compared with the results from BP-PAM, the reconstructed signal (optical absorption) amplitudes and distribution using CS-PAM also agrees better with that of the corresponding in-focus hair images (the assumed gold standard). To further demonstrate this improvement, the maximum amplitude projections (MAP, along z -axis) of the B-scan images are plotted in Fig. 3 for comparison. These plots confirm that, overall, CS-PAM has provided better contrast-to-noise ratio (CNR) and spatial resolution over BP-PAM. In one particular case [Fig. 3(d)], in which the hairs are seriously out of focus, CS-PAM has offered ~ 4 -fold improvement in CNR and $\sim 10\%$ improvement in spatial resolution, compared with that of BP-PAM.

3.2 In Vivo Results

To validate the performance of CS-PAM *in vivo*, the back of an anesthetized nude mouse weighing $\sim 25 \text{ g}$ was imaged. The transducer height was varied in experiments, so that two photoacoustic images were acquired, first when the skin surface of the mouse back was in focus, and then when it was $\sim 4\text{-mm}$ out of focus. The laser (at 570 nm) fluence used in this study was $\sim 2 \text{ mJ/cm}^2/\text{pulse}$ on the skin surface, well below the 20-mJ/cm^2 American National Standards Institute laser safety limit. All animal experiments described here were carried out in compliance with the approved protocols of Shenzhen Institutes of Advanced Technology, Chinese Academy of Sciences.

The image acquired when the mouse back was in focus is assumed as the gold standard [Fig. 4(a)], while the directly acquired PAM image when the mouse back was out of focus

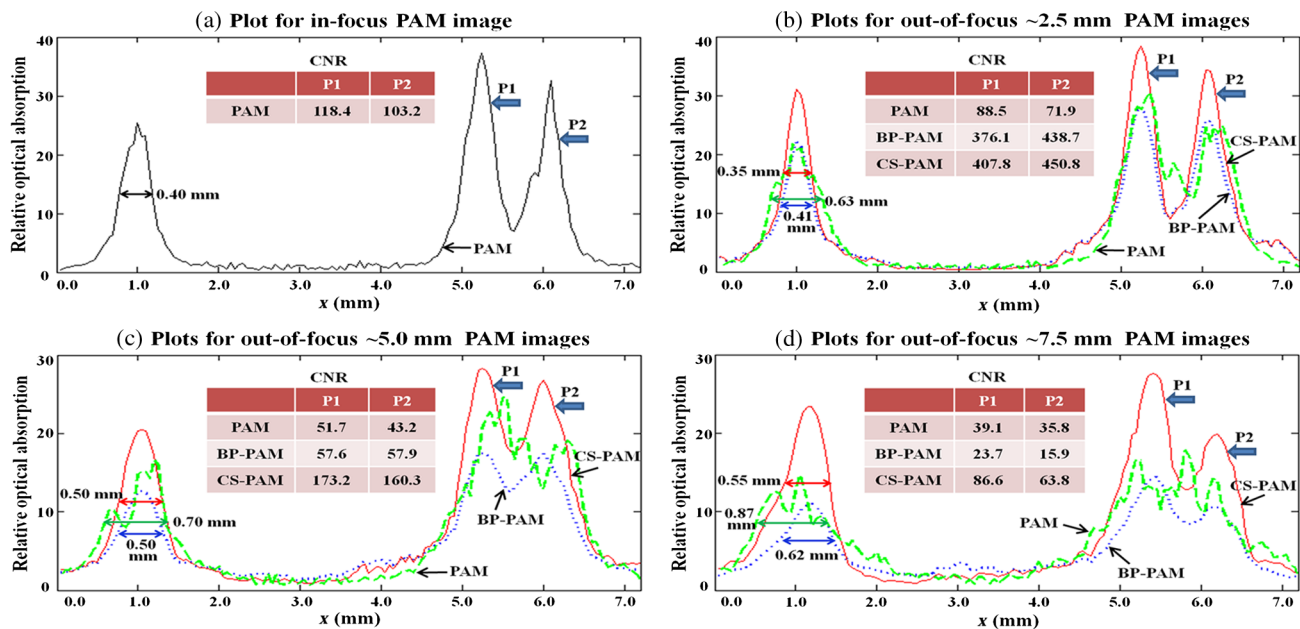


Fig. 3 Plots of the maximum amplitude projections (MAP) of the hair phantom's B-scans. The three peaks from left to right represent the MAP plots of hairs 1, 2, and 3, respectively. (a) Plot (from directly acquired PAM image) with the phantom at the focal point; (b)–(d) Plots with the phantom at ~ 2.5 , 5, and 7.5 mm away from the focal point, respectively. The arrows indicate the FWHMs of the peaks; CNR, contrast-to-noise ratio.

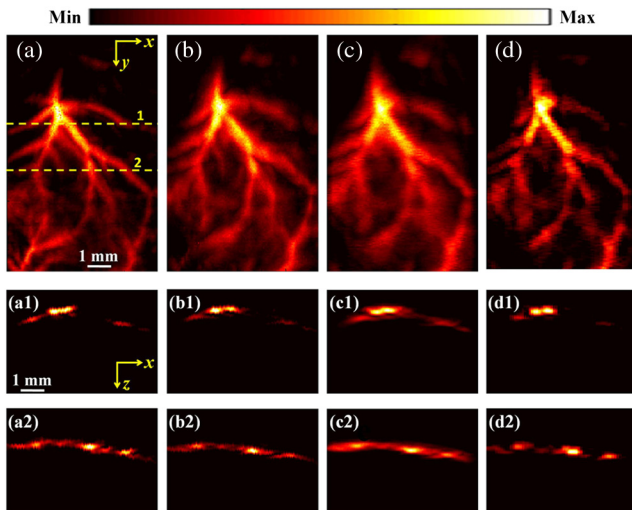


Fig. 4 *In vivo* PAM of the back of a mouse. (a) Directly acquired PAM image with the skin surface in-focus; (b) directly acquired PAM image with the skin surface ~ 4 mm out-of-focus; (c) and (d) Recovered images when the skin surface is ~ 4 mm out-of-focus, using BP-PAM and CS-PAM, respectively. (a1)–(d1) and (a2)–(d2) B-scans corresponding to the cross sections along line 1 and line 2, respectively, in (a).

is shown as a control [Fig. 4(b)]. Figures 4(c) and 4(d) show the corresponding image reconstructed with BP-PAM and CS-PAM, respectively. Note that the images in Figs. 4(a)–4(d) are shown as the MAP—the maximum photoacoustic amplitudes projected along the depth direction toward the skin surface. To further compare the reconstructed images, representative B-scan images corresponding to the cross sections as indicated by dash lines 1 and 2 in Fig. 4(a) are also shown [Figs. 4(a1)–(d1) and (a2)–(d2)]. In all *in vivo* experiments, the comparison between BP-PAM and CS-PAM reconstructions was performed using identical sparse sampling data, acquired with a scanning step size of $50 \mu\text{m}$. Through *in vivo* imaging, we can see that: (1) similar to that in the phantom experiments, the directly acquired PAM images of the out-of-focus targets (mouse-back vessels) were both blurred and of degraded CNR [Fig. 4(b)]; (2) in contrast to that in the phantom experiments, BP-PAM did not provide obvious improvement in image quality for the out-of-focus targets *in vivo*; and (3) CS-PAM essentially maintained its great performance in improving the image quality in the *in vivo* case. Presumably, the deteriorated performance of BP-PAM *in vivo* was due to the small divergence angle of the virtual detector, together with the relatively low CNR (compared with that in the phantom experiments). In CS-PAM, however, the use of the CS-based reconstruction model has partially compensated the effect of the small divergence angle.¹³

4 Discussion and Conclusions

In this proof of concept study, there were still factors that posed limitations to the performance of CS-PAM. First, as in most PAM systems, the FWHM of the focal point (~ 0.25 mm) of the focused ultrasonic transducer was significantly larger than $\lambda_0/2$, which did not meet the assumption of “point-like” virtual detector. Second, the ultrasonic transducer was spherically focused (the virtual detector had a cone-shaped detection volume), while the image reconstruction was performed on each B-scan cross section. As a result, the received signals from

out of the B-scan plane would interfere with the two-dimensional reconstruction. In future, to overcome the first limitation, a new model to treat the virtual detector as a finite-size element, similar to that in IMMI, needs to be developed;⁷ to overcome the second limitation, the development of a new volumetric reconstruction model can be a potential solution. However, even under these restrictions, CS-PAM has still enabled significant improvement in image quality of the out-of-focus regions, compared with that in either conventional PAM or BP-PAM.

In summary, a CS-PAM has been developed. Phantom and *in vivo* experiments have demonstrated that CS-PAM can effectively extend the depth of focus of conventional PAM. In addition, compared with the conventional back projection–based virtual-detector photoacoustic microscopy (BP-PAM), CS-PAM has offered finer spatial resolution, higher CNR, and more accurate signal amplitude distribution in the recovered images. The results shown in this study suggest that CS-based photoacoustic reconstruction in conjunction with the virtual detector technique can be an effective way to extend the imaging range of PAM, and thus may greatly expand its biomedical applications.

Acknowledgments

This work was supported in part by the National Natural Science Foundation of China Grants Nos. 61308116 and 61205203, the National Key Basic Research (973) Program of China 2014CB744503, the Ministry of Science and Technology of China Grant No. 2014DFG32800, and the Shenzhen Science and Technology Innovation Committee Grants Nos. ZDSY20130401165820357, KQCX20120816155844962, CXZZ20120617113635699, and JCYJ20120615125857842.

References

1. L. V. Wang and S. Hu, “Photoacoustic tomography: *in vivo* imaging from organelles to organs,” *Science* **335**(6075), 1458–1462 (2012).
2. M. Heijblom et al., “Visualizing breast cancer using the Twente photoacoustic mammoscope: what do we learn from twelve new patient measurements?,” *Opt. Express* **20**(11), 11582–11597 (2012).
3. L. Song et al., “Ultrasound-array-based real-time photoacoustic microscopy of human pulsatile dynamics *in vivo*,” *J. Biomed. Opt.* **15**(2), 021303 (2010).
4. H. F. Zhang et al., “Functional photoacoustic microscopy for high-resolution and noninvasive *in vivo* imaging,” *Nat. Biotechnol.* **24**(7), 848–851 (2006).
5. C. Kim et al., “*In vivo* molecular photoacoustic tomography of melanomas targeted by bioconjugated gold nanocages,” *ACS Nano* **4**(8), 4559–4564 (2010).
6. L. Wang, K. Maslov, and L. V. Wang, “Single-cell label-free photoacoustic flowoxigraphy *in vivo*,” *Proc. Natl. Acad. Sci. U. S. A.* **110**(15), 5759–5764 (2013).
7. L. Wang et al., “Ultrasonically encoded photoacoustic flowgraphy in biological tissue,” *Phys. Rev. Lett.* **111**(20), 204301 (2013).
8. M. L. Li et al., “Improved *in vivo* photoacoustic microscopy based on a virtual-detector concept,” *Opt. Lett.* **31**(4), 474–476 (2006).
9. M. A. A. Caballero et al., “Model-based photoacoustic imaging using focused detector scanning,” *Opt. Lett.* **37**(19), 4080–4082 (2012).
10. C. Kim et al., “Objective-free optical-resolution photoacoustic microscopy,” *J. Biomed. Opt.* **18**(1), 010501 (2013).
11. D. L. Donoho, “Compressed sensing,” *IEEE Trans. Inf. Theory* **52**(4), 1289–1306 (2006).
12. J. Meng et al., “*In vivo* optical-resolution photoacoustic computed tomography with compressed sensing,” *Opt. Lett.* **37**(22), 4573–4575 (2012).
13. J. Meng et al., “Compressed-sensing photoacoustic computed tomography *in vivo* with partially known support,” *Opt. Express* **20**(15), 16510–16523 (2012).

14. Z. Sheng et al., "Protein-assisted fabrication of nano-reduced graphene oxide for combined *in vivo* photoacoustic imaging and photothermal therapy," *Biomaterials* **34**(21), 5236–5243 (2013).
15. M. Xu and L. V. Wang, "Universal back-projection algorithm for photoacoustic computed tomography," *Phys. Rev. E* **71**(1), 016706 (2005).
16. J. Provost and F. Lesage, "The application of compressed sensing for photo-acoustic tomography," *IEEE Trans. Med. Imaging* **28**(4), 585–594 (2009).
17. Z. J. Guo et al., "Compressed sensing in photoacoustic tomography *in vivo*," *J. Biomed. Opt.* **15**(2), 021311 (2010).
18. M. Lustig, D. Donoho, and J. M. Pauly, "Sparse MRI: the application of compressed sensing for rapid MR imaging," *Magn. Reson. Med.* **58**(6), 1182–1195 (2007).

Jing Meng is an associate professor at the Qufu Normal University. She received her BS and MS degrees in mathematics from Qufu Normal University in 1999 and 2003, respectively, and her PhD degree in computer engineering from Soochow University in 2006. She has engaged in photoacoustic imaging as a research fellow at the Shenzhen Institutes of Advanced Technology, Chinese Academy of Sciences since 2011.

Chengbo Liu is an assistant professor at the Research Lab for Biomedical Optics and Molecular Imaging at Shenzhen Institutes of

Advanced Technology, Chinese Academy of Sciences. Prior to joining SIAT, he received his PhD degree in biomedical engineering from Xi'an Jiaotong University. During his PhD training, he spent 2 years at Duke University working on tissue spectroscopy.

Jiaxiang Zheng is a research assistant at the Research Lab for Biomedical Optics and Molecular Imaging at Shenzhen Institutes of Advanced Technology, Chinese Academy of Sciences. Prior to joining SIAT, he received his MS degree in biomedical engineering from Tianjin University, China.

Riqiang Lin is an assistant professor at the Research Lab for Biomedical Optics and Molecular Imaging at Shenzhen Institutes of Advanced Technology, Chinese Academy of Sciences. Prior to joining SIAT, he received his MS degree in mechanical engineering from Shenzhen University, China.

Liang Song is an associate professor and founding director of the Research Lab for Biomedical Optics and Molecular Imaging at the Shenzhen Institutes of Advanced Technology, Chinese Academy of Sciences. Prior to joining SIAT, he studied at Washington University in St. Louis with Professor Lihong Wang and received his PhD degree in biomedical engineering in 2010.